ISPRS Journal of Photogrammetry and Remote Sensing 210 (2024) 55–68

Contents lists available at ScienceDirect

ISPRS Journal of Photogrammetry and Remote Sensing

journal homepage: www.elsevier.com/locate/isprsjprs

Evaluation of Landsat-9 interoperability with Sentinel-2 and Landsat-8 over Europe and local comparison with field surveys

F. Trevisiol , E. Mandanici *, A. Pagliarani , G. Bitelli

Department of Civil, Chemical, Environmental and Materials Engineering (DICAM) - University of Bologna, Viale del Risorgimento 2, 40136 Bologna, Italy

ARTICLE INFO

Keywords:
Landsat-9
Harmonization
Field-survey
Cross-sensor comparison
Time-series

ABSTRACT

The recent launch of Landsat-9 satellite enriches the opportunities to work with dense time series of multispectral medium-resolution images. The integration of Landsat-9 in a multi-constellation series with Landsat-8 and Sentinel-2 requires a harmonization of the surface reflectance values that can be obtained from the official Level-2 products. This paper proposes the coefficients of the optimal linear transformations for the European continent, which allow to integrate Landsat-9 with the similar operating missions. These coefficients are based on a regression over 30 independent random extractions of 240,000 samples from images of the same areas but acquired by different sensors within two days. The coefficients were validated on an independent dataset. Furthermore, the effects of the proposed harmonization were tested on four popular vegetation indices, by evaluating the distributions of the differences in values obtained from each sensor pair. Finally, a test on a local scale was carried out with a spectroradiometer survey on 16 locations to collect some reference spectra to be compared with the reflectance values provided by the images. The results demonstrate the interoperability of Landsat and Sentinel-2 missions, since reflectance differences are in most cases within the accuracy specifications of the sensors. However, some discrepancies are observed in the blue and SWIR bands, probably due to inconsistencies in the atmospheric correction processes.

1. Introduction

After its successful launch in September 2021 and a calibration period, Landsat-9 (L9) data were made available for download for the first time on February 15, 2022. This new dataset increases as never before the number of Landsat-like satellites in orbit, representing a great potential for data availability and suitability for several applications (Wulder et al., 2022). Indeed, as evidenced by the study of Li and Chen (2020), the combined use of L9 in a virtual constellation with Landsat-8 (L8) still operating and the twin Sentinel-2 (S2) satellites allows to reach a 2.3 days revisit time. This achievement is vital for end-users requiring cloud-free data for monitoring purposes, providing more than three observations per week (Li & Roy, 2017; Wu et al., 2019) and reducing the data gaps and noise due to atmospheric effects, such as clouds and haze (Ghaderpour & Vujadinovic, 2020).

This awareness led to the design of the Landsat and Sentinel-2 missions with great sensors similarity, enabling interoperability. However, some elements, such as satellite orbits and acquisition geometry (illumination and view angles), may limit their consistency. This is the case, for example, of the orbit drift of Landsat-7 (L7) and Landsat-5, which introduced discrepancies in data coherence that had to be evaluated (Qiu et al., 2021; Zhang & Roy, 2016).

Furthermore, both Sentinel and Landsat missions are committed to deliver different product levels for different users (Wu et al., 2019; Wulder et al., 2019). Beside the standard Level-1 products (Top-Of-Atmosphere, TOA), surface reflectance (Bottom-Of-Atmosphere, BOA) datasets are delivered as Level-2 images corrected for the atmospheric effects. In general, for monitoring or change detection studies, the use of BOA is required to avoid false change detections due to different atmosphere conditions. However, the official reflectance products are obtained by Landsat and Sentinel-2 missions through different atmospheric correction algorithms, each of them laying on different auxiliary data for the estimation of atmosphere parameters, such as water vapour, pressure or aerosol optical thickness (Main-Knorn et al., 2017; Vermote et al., 2016).

For these reasons, it is important to assess the consistency of the BOA datasets among these missions to ensure data continuity. Moreover, as recommended by Helder et al. (2018), cross-calibration comparisons

* Corresponding author.
E-mail address: emanuele.mandanici@unibo.it (E. Mandanici).

https://doi.org/10.1016/j.isprsjprs.2024.02.021
Received 7 September 2023; Received in revised form 28 January 2024; Accepted 29 February 2024
Available online 10 March 2024
0924-2716/© 2024 The Author(s). Published by Elsevier B.V. on behalf of International Society for Photogrammetry and Remote Sensing, Inc. (ISPRS). This is an open access article under the CC BY license (http://creativecommons.org/licenses/by/4.0/).

between Landsat and S2 should be promoted to improve data interoperability and they should include BOA as well as TOA observations. The authors also suggest implementing these studies on a regular basis, which is even more crucial for calibration purposes of new satellites, like in the case of L9.

In order to assess cross-sensor discrepancy and build a virtual constellation, some authors proposed transformations of reflectance values to account for spectral and angular residual differences. Recently, Gross et al. (2022) used the underfly event during the launch of the L9 to compare its observations to those acquired by L8 from almost the same point of view and provided the first calibration parameters for L9. Mandanici and Bitelli (2016) performed a limited image-to-image S2 and L8 comparison between corresponding bands, while Roy et al. (2016) computed statistical coefficient to harmonize TOA and BOA of L7 and L8 considering the entire United States. Chastain et al (2019) extended this approach in a cross-sensors comparison of S2 MultiSpectral Instrument (MSI), L8 Operational Land Imager (OLI), and L7 Enhanced Thematic Mapper Plus (ETM +) top of atmosphere spectral bands, giving the regression coefficients to build a multi-mission synthetic constellation.

To mitigate the problems derived from different atmospheric correction algorithms and bidirectional reflectance distribution functions (BRDF) of the surfaces, NASA started distributing a collection of Harmonised Landsat Sentinel-2 (HLS) products in 2018, with the aim of creating a virtual constellation (Claverie et al., 2018). The collection is now at version 2 and provides MSI and OLI products resampled at 30 m in the spatial grid of S2 (U.S. Geological Survey, 2021). Quality control is still in progress, but the overall relative uncertainty in a single band reflectance (except blue one) is expected to be lower than 11 % (Claverie et al., 2018). A study on time series (TS) in Canada suggested a better performance of HLS data over non-vegetated areas, especially at higher latitudes (Wulder et al., 2021), possibly in relation to residual BRDF issues.

Very few studies included comparisons with in-situ survey. Marujo et al. (2021) compared L8 and S2 observations with *in situ* measurements collected in Brazil in order to assess the impact of the two atmospheric correction algorithms. Instead, Teixeira Pinto et al. (2020) focused on the Landsat mission: they presented a radiometric performance evaluation of L7 and L8 products supported by surveys from eight test sites located in four different continents. At the time of the writing, the authors could not find any study including cross-sensors comparison of L8/L9 with S2 observations at continental level, supported by *in situ* data.

Therefore, the present study proposes a methodology to compile a robust collection of reflectance samples from imagery and estimate the coefficients of a linear transformation for the harmonization of the L8, L9 and S2 data. This linear transformation is expected to be valid all over the European continent and is designed to be applied on official level-2 satellite products, in order to ease the implementation for end-users including non-experts.

Furthermore, the effects of the proposed harmonization were tested computing four of the most popular vegetation indexes starting from the harmonized spectral bands of the considered sensors.

Finally, a comparison between reflectance values extracted from images and contemporary spectral signatures measured on the ground by a spectroradiometer is performed on a local scale, to investigate discrepancies in reflectance values among the different multispectral sensors.

All the experiments are based on the identification of dates when all the considered satellites (L8, L9 ad S2) capture an image of the same area in two days maximum. These concurrences are called here COEs (Contemporary Overpass Event). The following sections details the methodology adopted and the obtained results.

2. Materials and methods

2.1. Sensor characteristics

For the present study, BOA and TOA products derived from Landsat-9, Landsat-8 and Sentinel-2 were compared. L8 and L9 orbit around the Earth at a nominal altitude of 705 km, crossing the equator on the descending node at 10:00 (±15 min) a.m. Mean Local Time (MLT), with a revisit cycle of 16 days each (8 days considering both platforms). The orbit of Sentinel-2 satellites is 786 km high and crosses the equator at 10:30 (±15 min) a.m. Mean Local Solar Time at the descending node (ESA, 2015b).

OLI and MSI, onboard L8 and S2 respectively, acquire images with a radiometric resolution of 12-bits, while L9 OLI-2 stores information using 14-bits. Finally, all the products are delivered as 16-bit digital images (ESA, 2015b; Gross et al., 2022; U.S. Geological Survey, 2022b). OLI and S2 have 11 and 13 bands, respectively; however, only the six bands which share comparable spectral characteristics were considered here. These are Blue, Green, Red, NIR, SWIR1 and SWIR2 bands (Table 1). Indeed, the percentages of overlap in per-band Spectral Response Functions (SRF) among the Sentinel-2 MSI and Landsat OLI were estimated as follows by Chastain et al. (2019): Blue 79.2 %, Green 99.5 %, Red 78.1 %, NIR (Band-8a) 98.8 %, SWIR1 89.7 % and SWIR2 92.2 %, and OLI-2 has been designed to be as similar as possible to OLI.

A relevant difference between the missions is the different atmospheric correction algorithm adopted in the generation of Level-2 products, i.e. the Land Surface Reflectance Code (LaSRC) algorithm (Vermote et al., 2016) for Landsat and the Sen2Cor processor (Main-Knorn et al., 2017) for S2. LaSRC estimates atmospheric constituents from ancillary data (climate information from MODIS, SRTM) and retrieves the aerosol concentration from the blue band. Sen2Cor instead estimates the atmosphere aerosol parameters using the Dense Dark Vegetation algorithm (Kaufman & Sendra, 1988); while the water vapour retrieval is performed with the Atmospheric Pre-corrected Differential Absorption algorithm (Schläpfer et al., 1998).

2.2. Computation of harmonization coefficients at continental level

To collect the data required for the cross comparison, a dedicated workflow (Fig. 1) for image pre-processing and sample extraction was implemented in the Google Earth Engine (GEE) platform through the Javascript API (Gorelick et al., 2017). The considered image collections provided in the GEE data catalog are the L9 and L8 Collection-2 Tier-1 TOA and BOA, and the Harmonized Sentinel-2 TOA and BOA datasets, which are already corrected for the shift in DN introduced with the processing baseline 04.00 (ESA, 2015a).

Moreover, a land cover dataset was included in the analysis. In particular, GEE offers the Dynamic World Land Use Land Cover (DWLULC) (Brown et al., 2022), which provides a 10 m resolution map, obtained from the classification of every S2 image and associated to it. It is based on a deep-learning algorithm that discriminates the following classes: water, trees, grass, flooded vegetation, crops, shrub and scrub, built area, bare ground, snow and ice. This dataset was selected for its

Table 1
Comparison of the similar spectral bands of the MSI, OLI-2 and OLI instruments.

Landsat-8/9 OLI/OLI-2			**Sentinel-2 MSI**		
Bands	*Wavelength (μm)*	*Res. (m)*	*Bands*	*Wavelength (μm)*	*Res. (m)*
B2 Blue	0.450—0.510	30	*B2 Blue*	0.458—0.523	10
B3 Green	0.533—0.590	30	*B3 Green*	0.543—0.578	10
B4 Red	0.636—0.673	30	*B4 Red*	0.650—0.680	10
B5 NIR	0.851—0.879	30	*B8a NIR*	0.855—0.875	20
B6 SWIR-1	1.566—1.651	30	*B11 SWIR-1*	1.565—1.655	20
B7 SWIR-2	2.107—2.294	30	*B12 SWIR-2*	2.100—2.280	20

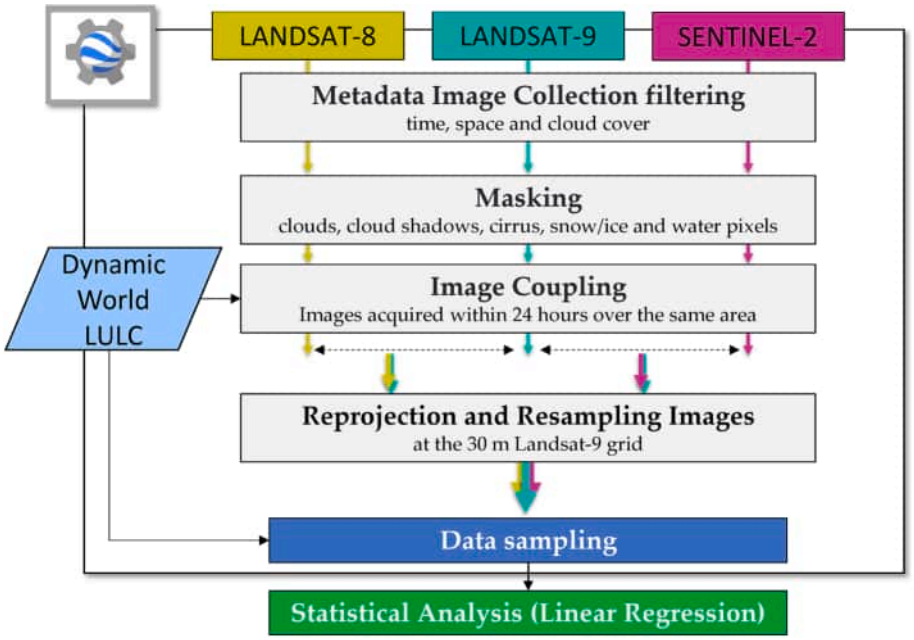

Fig. 1. Workflow of the harmonization coefficients computation.

high spatial resolution and temporal coherence with every S2 image.

The three sensors were compared in pairs, by randomly sampling the pixel values from triplets of overlapping images sensed with a maximum delay of one day from the L9 acquisition, as detailed in the following sections. The final statistical analysis on the sampled data was computed in Python environment.

2.2.1. Study area

The analysis was performed over the entire European continent. The total area was tiled into subregions in order to reduce as much as possible the computational burden. Since the reliability of the BOA products is ensured for a latitude lower than 65° (Campbell & Aarup, 1989; U.S. Geological Survey, 2019), the analysis excluded regions at higher latitude (Fig. 2).

2.2.2. Data gathering and preparation

First of all, the archives of the three sensors were filtered separately based on metadata, which include time, space and cloud cover. For each collection, all the images acquired from 1 February 2022 until December 2022, over Europe, with a cloud coverage lower than 15 % were selected. This threshold was set to gather a sufficient number of good quality images, but considering the very recent availability of L9. Overall, 3,826 L8, 3,765 L9 and 48,664 S2 images satisfied these filters. Moreover, every S2 image was joined with the associated land use land cover provided by the DWLULC dataset. At this point, the images remaining after the previous filtering were pixel-wise masked using the pixel quality assessment (QA) bitmask band and Scene Classification map (SCL) quality assessment band for Landsat and S2 respectively (Foga et al., 2017; Louis et al., 2010). These products, which are automatically generated by level-2 algorithms and delivered in the final products as additional bands, were used to remove high and medium

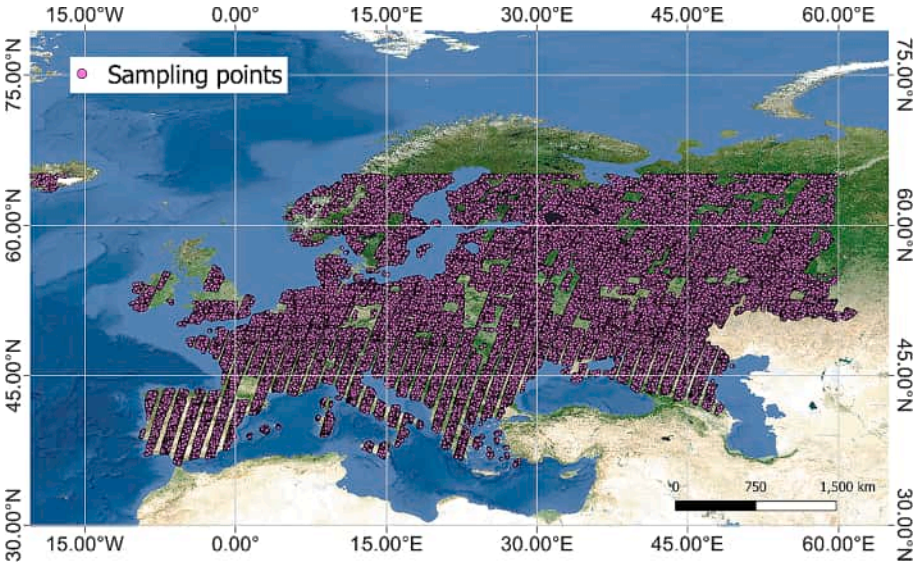

Fig. 2. Area covered by the cross-sensors comparison and distribution of random sampling. Basemap: Sentinel-2 cloudless - https://s2maps.eu by EOX IT Services GmbH.

confidence clouds, dilated clouds, cloud shadows, high confidence cirrus, snow/ice and water pixels. In addition, saturated and out-of-range pixels were masked out.

2.2.3. Image pairing, co-registration and reprojection

The filtered images of two different sensors (L8 with L9 and S2 with L9), which are spatially overlapping and acquired within 24 h, were paired, finely co-registered and resampled at the L9 grid. S2 was aggregated at 30 m by computing the mean values of the original 10 or 20 m pixels; while the DWLULC map was subsampled using the mode statistics.

At this point, an additional mask was calculated to exclude possible residual changes in land cover that might be occurred between the two acquisitions of the paired images. The mask was calculated on the pixel-wise difference in the blue band values, following the methodology proposed by Roy et al. (2016). Pixels with a difference in the blue greater than the 50 % of their mean were discarded. It was assumed that such a change in the blue can be caused by surface changes or by the presence of undetected clouds and therefore masked out from the analysis.

Finally, the two paired collections were merged together through an inner join operation, selecting those L8/L9 and S2/L9 pairs sharing the same Landsat-9 image. The resulting collection is made of 22,256 triplets of images acquired in the same area by L8, S2 and L9, where L8 and S2 were acquired at a maximum distance of 1 day from the L9. Also the masks were merged, to keep only the pixels with valid values in all the images.

2.2.4. Data sampling

From the obtained image triplets, a large number of pixels were randomly extracted to perform the cross-sensor comparisons. A stratified sampling approach was applied based on the land cover classes, in order to extract a representative sample from each class. Different sample sizes were tested and it was observed that significant and stable results can be obtained with a size greater than 240,000 observations. Therefore, 30 independent extractions of about 240,000 sample pixels were performed. The size of each single extraction might slightly differ because a post-extraction check and duplicates removal were conducted.

For every pixel, both TOA and BOA values were extracted for the six common bands. Then, the differences in reflectance between almost synchronous L8 and L9 observation and between S2 and L9 were computed and statistically analysed.

Finally, a further independent extraction was performed to build a validation dataset to test the coefficients of the cross sensor analysis. In this case, the selected sample size is more than double the single extraction and about 10 % of the entire training dataset.

2.2.5. Cross-sensors analysis

A linear model was estimated to harmonize atmospherically corrected BOA values from different sensors. For each couple (S2/L9 and L8/L9) two Ordinary Least Square (OLS) regressions and a Reduced Major Axis (RMA) regression were computed (Harper, 2016).

In the classic OLS approach, the slope and intercept values change depending on which variable (i.e., which sensor) is defined as dependent; thus, OLS was performed twice by switching the variables (Roy et al., 2016). Conversely, the RMA regression considers both the dependent and independent variables as affected by errors, which is more realistic in this context because all the sensors can be affected by calibration errors (Chastain et al., 2019; Roy et al., 2016). The obtained relationship, in this case, can be inverted with a simple algebraic operation (Harper, 2016).

The goodness of the fit was evaluated with the coefficient of determination (r^2), while the regressions significance was defined by the overall F-statistic p-value (Roy et al., 2016). The similarity of the sampled pair values was quantified using the Mean Difference (MD) and the Root Mean Square Deviation (RMSD), as defined in Chastain et al. (2019):

$$MD = \sum_{i}^{n} \frac{v_i^A - v_i^B}{n} \tag{1}$$

$$RMSD = \sqrt{\frac{\sum_{i}^{n} \left(v_i^A - v_i^B\right)^2}{n}} \tag{2}$$

Where v_i is the i-th pairwise pixel observation by generic sensor A or B, and n is the total amount of sampled pixels.

2.2.6. Vegetation indices

To test the obtained harmonization coefficients, some vegetation indices (VIs) were computed, since they are able to synthetize biophysical characteristics of vegetation. In particular, four of the most popular vegetation indices derived from the combination of Blue, Red, NIR and SWIR bands were considered: the Normalized Difference Vegetation Index (NDVI) (equation (3)), Soil Adjusted Vegetation Index (SAVI) (equation (4)), the Enhanced Vegetation Index (EVI) (equation (5)), and the Normalized Difference Moisture Index (NDMI) (equation (6)) (Trevisiol et al., 2024; Chaves et al., 2020).

$$NDVI = \frac{NIR - Red}{NIR + Red} \tag{3}$$

$$EVI = 2.5 \bullet \frac{NIR - Red}{NIR + 6 \bullet Red - 7.5 \bullet Blue + 1} \tag{4}$$

$$SAVI = 1.5 \bullet \left(\frac{NIR - Red}{NIR + Red + 0.5}\right) \tag{5}$$

$$NDMI = \frac{NIR - SWIR}{NIR + SWIR} \tag{6}$$

Firstly, the L9, S2 and L8 VIs were computed according to equations (3)–(6) for all the paired sampled BOA pixels. Secondly, the harmonized VIs were recomputed using the harmonized bands obtained through the application of the computed coefficients. In the following, the harmonized bands, sensors or vegetation indices are indicated with a small "h" before the name (e.g. hNDVI). Finally, for each cross-sensor comparison, the differences between NDVI, EVI, SAVI and NDMI values before and after harmonization were statistically analysed and compared. For example, the histogram of the differences in NDVI values derived from the original OLI-2 bands and the original MSI bands was compared with the histogram of the differences between the NDVI values computed from the original OLI-2 bands and the hNDVI values computed from the harmonised MSI bands. In this case, the harmonization is applied to MSI bands to improve their compatibility with the corresponding OLI-2 bands.

2.3. Local comparison with in-field survey

2.3.1. Survey design and study area

Among all the available image triplets, few were selected for a local analysis based on contemporary measurement of ground spectral signatures with a spectroradiometer. For practical and logistic reasons, two areas of interest (AOIs) were selected (Fig. 3). These areas are located in Italy, in the Emilia-Romagna region, one near Reggio-Emilia and the other near Ravenna. The two AOIs lie in the Po River valley, which is mainly characterised by intense agricultural activities.

Inside the selected AOIs, homogeneous surfaces of at least 120x120 m were identified as possible survey locations. Homogeneous, in this context, means a uniform type of land cover or material over the entire area, so that within it the spatial variability of the spectral signature is minimal. This characteristic, which was verified during field inspections, makes it easier to compare spot measurements on the ground and values extracted from image pixels (with a resolution of 10 or 30 m). The minimum extent comes from the need to address the effect of cubic

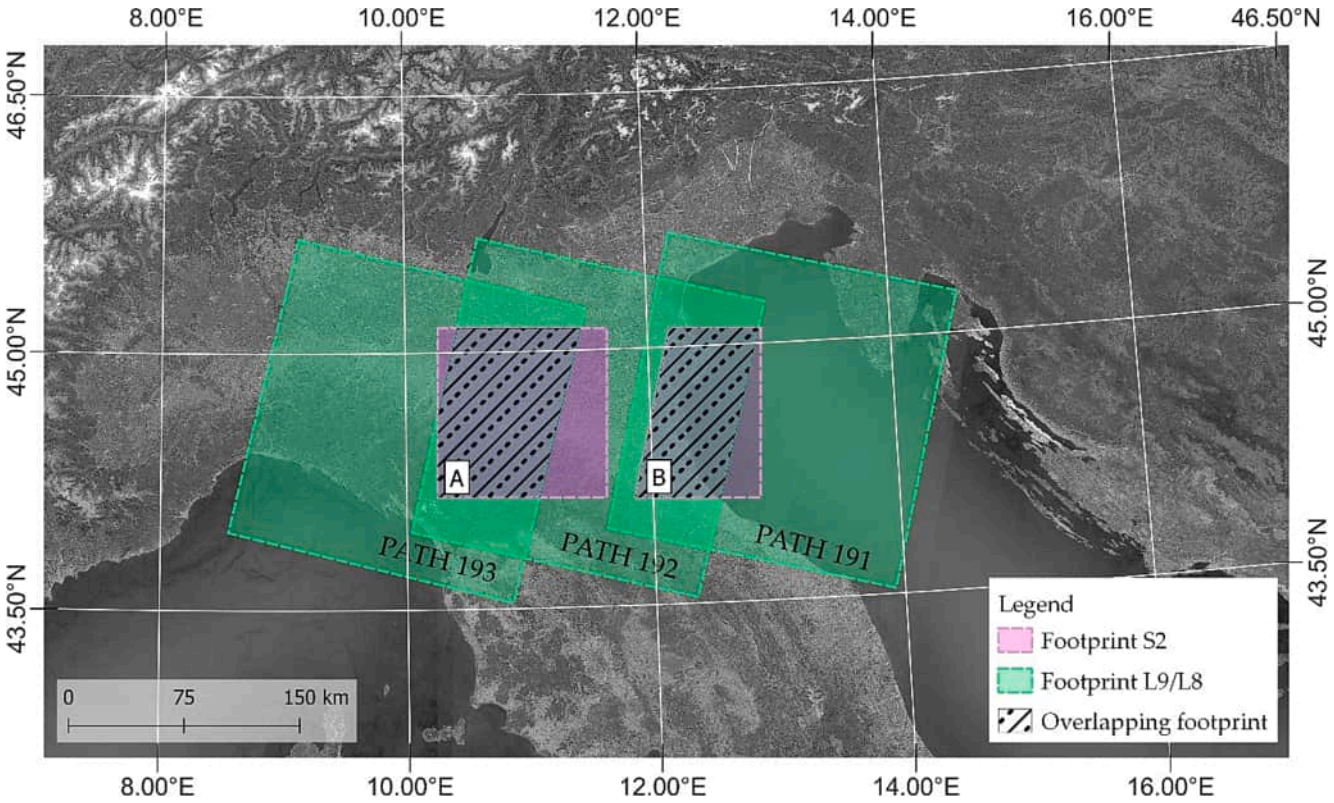

Fig. 3. Sentinel-2, Landsat-8/9 overlapping footprint in the Emilia-Romagna region in Italy: where surveys were conducted near Reggio Emilia (A) and Ravenna (B) cities. Basemap: Sentinel-2 cloudless - https://s2maps.eu by EOX IT Services GmbH.

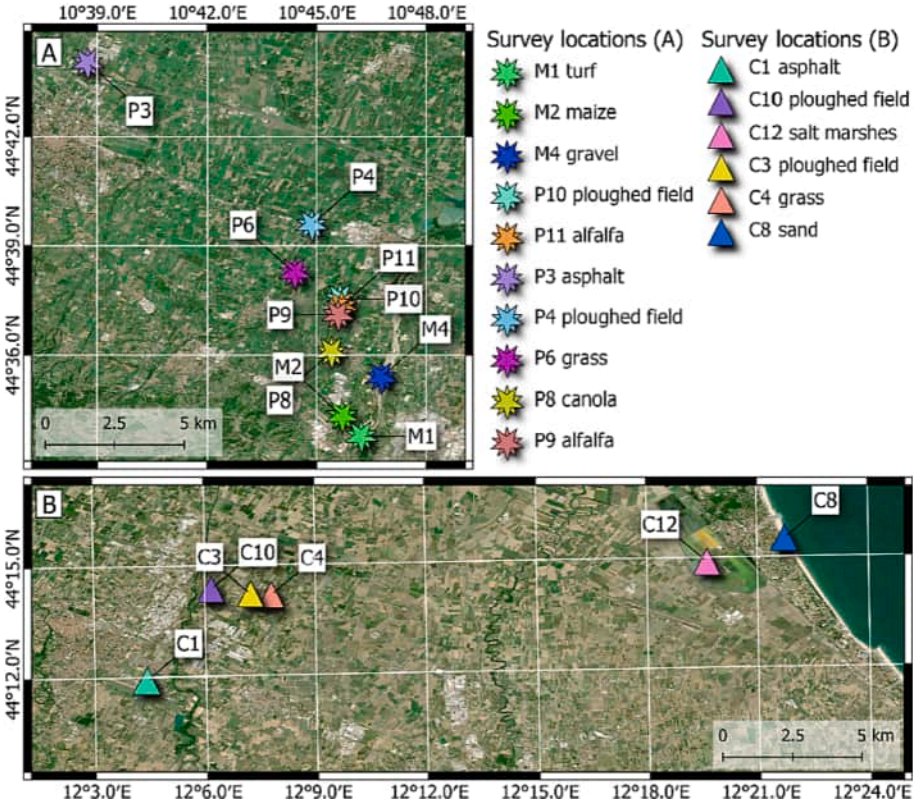

Fig. 4. Location of surveys and their land cover.

convolution (CC) applied during the orthorectification processing in the production of the official Level-1 data. Indeed, CC introduces some smoothing in the image, by averaging the spectra of nearby pixels covering heterogeneous surfaces. By isolating minimum 120x120 m^2 surfaces, which corresponds to a 4x4 Landsat pixels, the pixels in the middle should be less affected by this numeric effect. The selected extent is a trade-off between the need of wide homogeneous surfaces and the extremely patchy land cover of the Po valley. Moreover, the surveys aim to collect the spectral signatures of different types of surface, both anthropic and natural.

The time window to perform the ground measurements was limited to one hour before and one hour after the satellite image acquisitions. This choice is also a trade-off between the contrasting needs of limiting the variations of illumination conditions and of measuring as many spectra as possible. Therefore, the selected locations had to be spatially clustered. A further strong constraint is that it is only possible to operate in almost ideal weather conditions, i.e. clear skies, because the presence of scattered clouds or haze causes rapid fluctuations in irradiance. Finally, these locations needed to be open and accessible to public. Based on all these requirements, the sixteen points finally selected are shown in Fig. 4.

Table 2 provides a summary of the "Contemporary Overpass Events" (COE) that occurred in the selected AOIs, i.e. when S2, L8 and L9 captured the same site within 48 h one to the others and when, thanks to cloud-free weather conditions, the spectroradiometer surveys in the field were performed. For the selection of the dates also L8 was considered, but in the present study only the comparison between S2 and L9 was performed, because it is expected to be the most informative. Actually, further surveys were performed on 13 and 21 March 2022, but they could not be used due to an outage of the L9 thermal sensors and consequent unavailability of Level-2 products (U.S. Geological Survey, 2022a).

More details about the surveyed locations (coordinates and dates) can be found in the supplementary materials (SM7).

2.3.2. Spectroradiometer surveys

The spectroradiometer used in the survey is the SVC HR-768i by Spectra Vista Corporation. The instrument records spectra in the range 350 – 2500 nm with a high spectral resolution (768 channels). Details about the instrument characteristics can be found in Fig. 5a (Spectra Vista Corporation - SVC, 2019).

Table 2
Contemporary Overpass Events (COEs) details: date, platform and time of overpass over the same area.

COE	AOI	Date	Sensor	Orbit id	Path/ Row	Time (UTC)
A	Reggio Emilia	4/03/ 2022	L9		193/29	10:04
			S2	22-T32TPQ		10:10
		5/03/ 2022	L8		192/29	09:58
B	Reggio Emilia	28/04/ 2022	S2	22-T32TPQ		10:06
		29/04/ 2022	L8		193/29	10:04
		30/04/ 2022	L9		192/29	09:58
C	Ravenna	21/03/ 2022	L8		192/29	09:58
			S2	122-T32TQQ		10:00
		22/03/ 2022	L9		191/29	09:52
D	Ravenna	15/05/ 2022	S2	122-T32TQQ		10:00
		16/05/ 2022	L9		192/29	09:58
		17/05/ 2022	L8		191/29	09:52

At every location, a set of measurements was performed. The instrument was mounted on a monopod equipped with a ball head with a protractor. The measurements were taken at a height of about 1.5 m above the ground; therefore, the ground sampling distance is about 9 cm with the 4° optics and 30 cm with the 14° optics. At the beginning and at the end of a set, a calibrated Spectralon® panel was measured. Each set includes four readings with different inclinations in the nadir and two in the azimuth direction, for a qualitative evaluation of possible BRDF effects (Roitberg et al., 2022). Fig. 6 represents the adopted scheme for the set of measurements. At each site the set of measures was repeated in two distinct points (a compromise between the need to perform several measurements and the very limited time available).

2.3.3. Spectral signature processing

The collected spectral signatures underwent some pre-processing. The reflectance was corrected for the Spectralon® panel calibration curve and adjusted for little illumination variations during the execution of the set of readings. For each site, in the case of homogeneous material, the spectral signatures collected in the two points were simply averaged. In the case of ploughed fields where plants had sprouted, a linear mix was calculated between the soil and vegetation signatures (Fig. 7), with weights based on the percentage of vegetation cover. This percentage was roughly estimated from photographs taken in the field. Then, the signatures were resampled to the OLI-2 and MSI bands, using the relative SRFs of the sensors.

This procedure, implemented in ENVI-IDL environment, allows to compare these *in situ* measurements with satellite observations. Among the six spectra collected at every location, the two with the most similar elevation angle to the satellite acquisitions were averaged (see the skyplot in Fig. 6a). To do this, the acquisition angles of the satellites were extracted in every pixel from the metadata. While for Landsat-9 this information is already provided as an additional 30 m band, the Sentinel-2 angles were retrieved using the code provided by Pahlevan et al. (2017), modified to account for the new format of the quality masks introduced in baseline 4.00 processing (ESA, 2022a).

A comparison between the field spectra and the image spectra was performed for all the surveyed locations, considering here L9 and S2 only. The following indicators, widely adopted in the literature, were used to quantify the similarity between corresponding spectra:

- Spectral Angle Mapper (SAM): it calculates the angle between the positional vectors of two spectra in the feature space. The smaller this angle, the more similar the two compared spectra are (Kruse et al., 1993).
- Euclidean Distance (ED): it is the distance between two spectra in the feature space and it summarizes the reflectance difference in all the bands. The smaller the distance, the more similar the spectra.
- Spectral Correlation Angle (SCA): it is based on the conversion of the Pearson's correlation coefficient into an angle; the SCA ranges from 0 (full positive correlation) to 1.57 (full negative correlation) radians (Naresh Kumar et al., 2011; Robila & Gershman, 2005).
- Spectral information divergence (SID): it is a stochastic indicator that uses the probabilistic discrepancy of two spectra to quantify their similarity (Chang, 2000). The smaller the divergence, the more similar the spectra.

3. Results and discussion

3.1. European cross-sensors comparison

The results of the comparison between L9 and L8 and L9 and S2 are reported here. As described in Section 2.2, the statistics presented are obtained through 30 independent extractions for a total amount of more than 7 million of observations. For each band, the differences in reflectance between sensors and the mean linear regression coefficients are computed.

(a)	Spectroradiometer HR – 768i
Spectral range	350 nm – 2500 nm
Channels	768
Spectral resolution (FWHM)	≤ 3,5nm , 700nm ≤ 16,0 nm , 1500nm ≤ 14,0 nm , 2100 nm
FOV	4° , 16°
Radiometric calibration accuracy	± 5% @ 400nm ± 4% @ 700nm ± 7% @ 2200nm

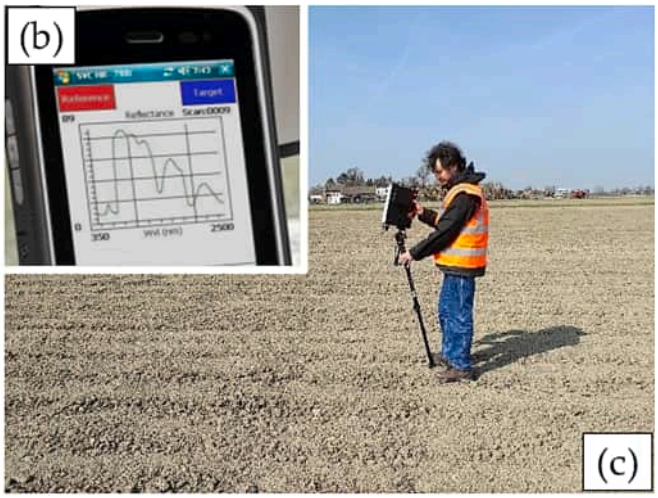

Fig. 5. A) spectroradiometer SVC HR-768i specifications; b) spectral signature as recorded by the spectroradiometer and displayed in the associated device; c) *in situ* measurement over a ploughed field.

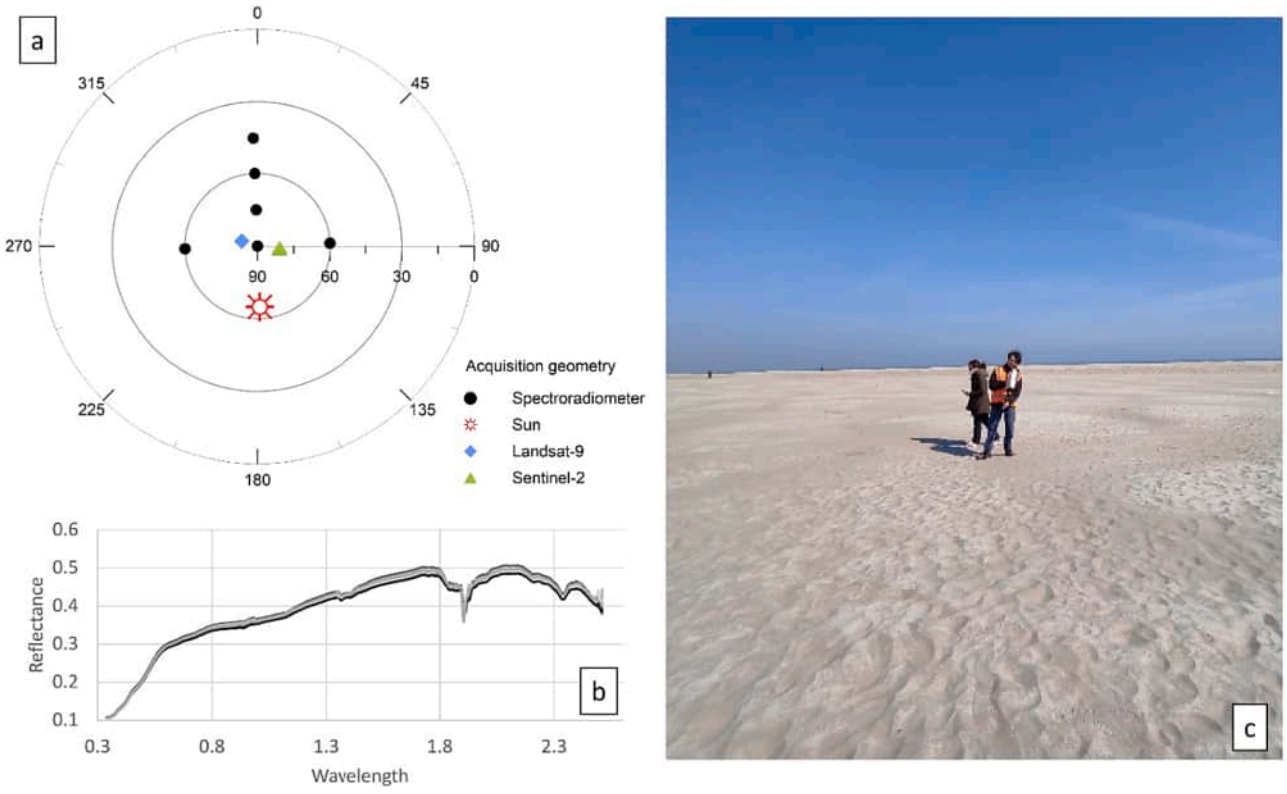

Fig. 6. The survey during COE D in C8 (sandy beach): (a) Skyplot of the designed acquisition geometry for the spectroradiometers measurements; (b) measured spectra; (c) a moment of the survey.

Analysing the differences in reflectance, it appears that the histograms of TOA and BOA differences are quite overlapping when considering L8 and L9, while they show differences when comparing L9 with S2 (Fig. 8 and supplementary materials SM1 and SM2). In this case, considering one extraction of the samples, the average difference in the TOA ranges between −0.0037 in the Blue and −0.0001 in the SWIR1 band; on the other hand, same values for BOA ranges from 0.0030 in the NIR to 0.0147 in the SWIR2.

This effect is likely to be related to the different atmospheric correction algorithms adopted by the two missions to produce the official Level-2 products. Moreover, some bands are more affected than others, such as the Blue, SWIR1 and SWIR2 bands. These bands, indeed, are those more affected by atmosphere elements such as water vapour and aerosol. However, it is important to remark that the analysis was performed with almost synchronous acquisitions and for this reason the TOA observations are so similar. This is not the case of TS analysis, which covers large time spans, and does require the use of BOA data.

Mean differences and root mean square deviations for BOA reflectance, for all the 30 independent extractions and for all the bands, are reported in Table 3. They confirm a great similarity between all the Level-2 products, with slightly more pronounced discrepancies between S2 and L9. In general, the dispersion of the differences in reflectance

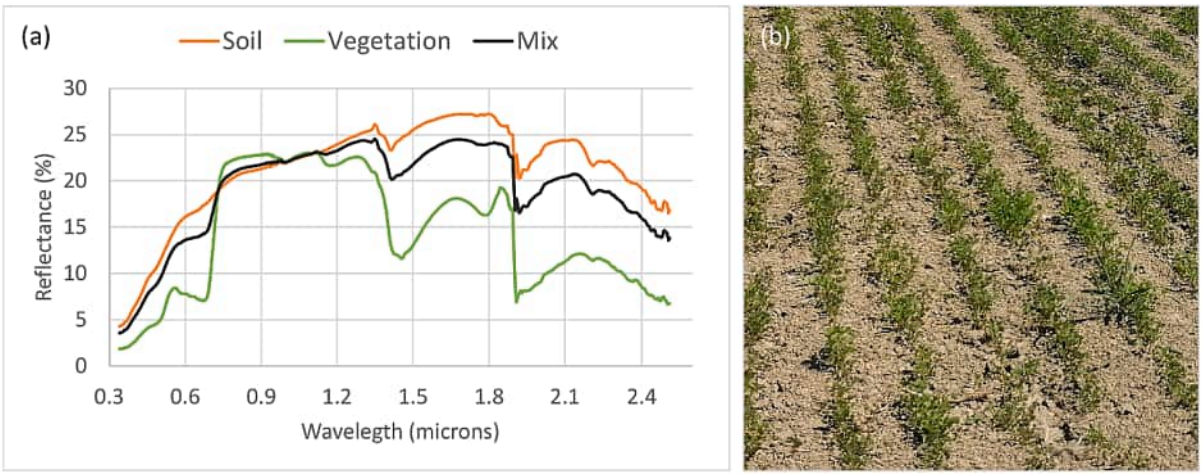

Fig. 7. Example of spectral signature mixing for the P4 site (COE B), where some plants had sprouted: (a) the original and mixed spectral signatures; (b) a field picture of the site.

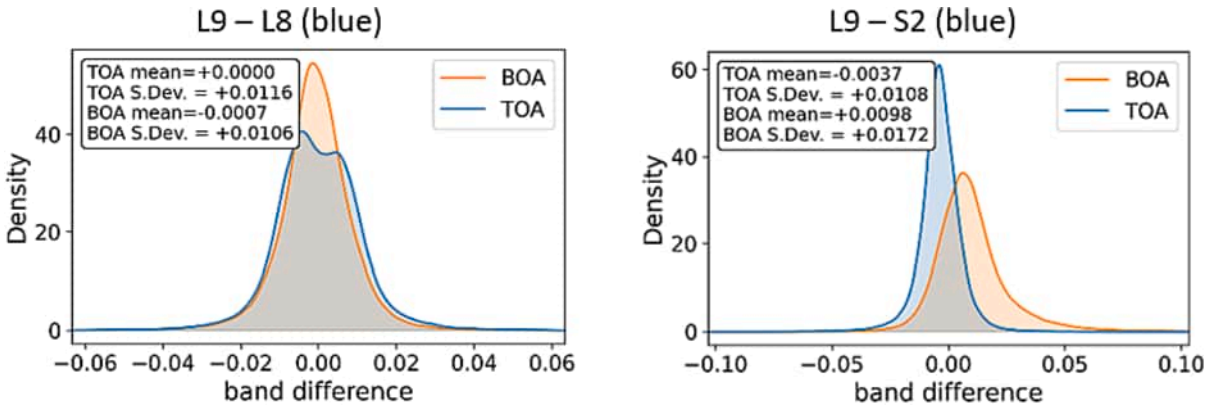

Fig. 8. Histograms of the differences in TOA and BOA reflectance values for the blue band between L8 and L9 (left) and L9 and S2 (right). Statistics for all the bands are given in the supplementary materials (SM1 and SM2) and refers to one extraction of 240,000 samples. (For interpretation of the references to color in this figure legend, the reader is referred to the web version of this article.)

Table 3
Statistics on the differences in BOA reflectance for all the 30 extractions of the samples.

	Landsat-8 – Landsat-9		Sentinel-2 – Landsat-9	
Band	**Mean Difference**	**Root Mean Square Deviation**	**Mean Difference**	**Root Mean Square Deviation**
Blue	−0.0005	0.0089	0.0093	0.0170
Green	−0.0014	0.0107	0.0038	0.0137
Red	−0.0009	0.0120	0.0055	0.0165
NIR	−0.0013	0.0233	0.0049	0.0276
SWIR1	−0.0021	0.0226	0.0139	0.0302
SWIR2	−0.0018	0.0179	0.0178	0.0288

comes from several factors: beyond the residual differences in sensor design, the main aspect may be the geometry of acquisition, the bi-directional reflectance functions of the surfaces, and the atmospheric correction for the Level-2 generation. The different orbits and sensing times of the Landsat and Sentinel satellites may result in measurements from distinct viewpoints and varying solar illumination conditions, even though the latter ones are minimal during COEs.

The next paragraphs present the regression analyses between L8 and L9 and L9 and S2 Level-2 products.

3.1.1. *Landsat-8 OLI and Landsat-9 OLI-2*

In Table 4 the results of the linear regression models are summarized. For every band the RMA and the two OLS transformation functions are reported, with the associated r^2 value. In general, the selected regression models well describe the dataset: $r^2 > 0.9$ and p-values < 0.0001 for all the bands. It seems that the best fitting is achieved from the cross-sensor analysis of the red bands, while the worst (r^2 equal to 0.9202) is in the blue linear regression. Likely, the blue wavelengths are highly affected by water vapour introducing noise in the sampled paired observations. This effect can be also seen in the scatterplots of Fig. 9 and supplementary material SM3. Indeed, in the scatterplot of the blue band (SM3a) the paired observations are concentrated around the identity axis just for a very short range of low values. After this low threshold, the paired data points begin to disperse for higher values, drawing a fan shape in the plot.

The independent validation dataset was used to assess the quality of the proposed solution. The differences between the paired observations before and after the application of the linear transformation were compared. In general, the difference between L8 and L9 is very low, and, as highlighted in Table 3, the similarity is higher in some bands. This can be seen in the histograms in Fig. 9 (and SM4), where the difference between original OLI and OLI-2 paired data are plotted together with the difference between the hOLI and OLI-2. hOLI is the OLI original observation harmonized to the OLI-2 by means of the computed transformation coefficients (Table 4). Overall, from the cross-sensors analysis

Table 4
Bands sensor transformation functions for Level-2 products (OLI to OLI-2 and OLI-2 to OLI): slope and intercept with their standard deviations in brackets, r^2 coefficient.

Landsat-8 OLI – Landsat-9 OLI-2 linear regressions (lat < 65°)			
Band	**Reg. type**	**Linear transformation function**	**r^2 (OLS)**
Blue	RMA	OLI-2 = 1.0078(±0.0015) OLI + 0.0001 (±0.0001)	0.9202
	OLS	OLI = 0.9518(±0.0015) OLI-2 + 0.0021 (±0.0001)	
	OLS	OLI-2 = 0.9668(±0.0015) OLI + 0.0023 (±0.0001)	
Green	RMA	OLI-2 = 1.0107(±0.0013) OLI + 0.0005 (±0.0001)	0.9352
	OLS	OLI = 0.9568(±0.0013) OLI-2 + 0.0024 (±0.0001)	
	OLS	OLI-2 = 0.9774(±0.0013) OLI + 0.0033 (±0.0001)	
Red	RMA	OLI-2 = 1.0103(±0.0010) OLI −0.0001 (±0.0001)	0.9583
	OLS	OLI = 0.9690(±0.0011) OLI-2 + 0.0021 (±0.0001)	
	OLS	OLI-2 = 0.9890(±0.0010) OLI + 0.0020 (±0.0001)	
NIR	RMA	OLI-2 = 1.0072(±0.0007) OLI −0.0007 (±0.0002)	0.9243
	OLS	OLI = 0.9545(±0.0007) OLI-2 + 0.0112 (±0.0002)	
	OLS	OLI-2 = 0.9684(±0.0007) OLI + 0.0099 (±0.0002)	
SWIR1	RMA	OLI-2 = 1.0082(±0.0009) OLI + 0.0001 (±0.0002)	0.9289
	OLS	OLI = 0.9560(±0.0009) OLI-2 + 0.0086 (±0.0002)	
	OLS	OLI-2 = 0.9717(±0.0009) OLI + 0.0089 (±0.0002)	
SWIR2	RMA	OLI-2 = 1.0145(±0.0012) OLI −0.0006 (±0.0002)	0.9478
	OLS	OLI = 0.9596(±0.0015) OLI-2 + 0.0048 (±0.0002)	
	OLS	OLI-2 = 0.9877(±0.0010) OLI + 0.0038 (±0.0002)	

performed between the Landsat satellites, it is clear that the two datasets differ just for a very little amount that is corrected by means of the transformation coefficient (see the two almost overlapping histograms for every band in SM4).

3.1.2. Sentinel-2 MSI and Landsat-9 OLI-2

All the results of the linear regressions are reported in Table 5, providing the transformation functions needed to harmonize the common spectral bands of L9 and S2 Level-2 products for a combined use. All

Table 5
Bands sensor transformation functions for Level-2 product (MSI to OLI-2 and OLI-2 to MSI): slope and intercept with their standard deviations in brackets, r^2 coefficient.

Sentinel-2 MSI and Landsat-9 (lat < 65°)			
Band	**Reg. type**	**Linear transformation function**	r^2
Blue	RMA	OLI-2 = 0.7819(±0.0022) MSI + 0.0044 (±0.0001)	0.9015
	OLS	MSI = 1.2143(±0.0036) OLI-2—0.0022 (±0.0002)	
	OLS	OLI-2 = 0.7424(±0.0021) MSI + 0.0069 (±0.0001)	
Green	RMA	OLI-2 = 0.8658(±0.0017) MSI + 0.0083 (±0.0001)	0. 9349
	OLS	MSI = 1.1168(±0.0025) OLI-2—0.0063 (±0.0002)	
	OLS	OLI-2 = 0.8371(±0.0016) MSI + 0.0109 (±0.0001)	
Red	RMA	OLI-2 = 0.8746(±0.0012) MSI + 0.0074 (±0.0001)	0. 9565
	OLS	MSI = 1.1182(±0.0017) OLI-2—0.0060 (±0.0001)	
	OLS	OLI-2 = 0.8554(±0.0011) MSI + 0.0093 (±0.0001)	
NIR	RMA	OLI-2 = 0.9597(±0.0008) MSI + 0.0063 (±0.0002)	0. 9040
	OLS	MSI = 0.9907(±0.0012) OLI-2 + 0.0075 (±0.0003)	
	OLS	OLI-2 = 0.9125(±0.0009) MSI + 0.0195 (±0.0002)	
SWIR1	RMA	OLI-2 = 0.9600(±0.0012) MSI −0.0037 (±0.0003)	0. 9069
	OLS	MSI = 0.9920(±0.0017) OLI-2 + 0.0159 (±0.0004)	
	OLS	OLI-2 = 0.9143(±0.0010) MSI + 0.0081 (±0.0002)	
SWIR2	RMA	OLI-2 = 0.9122(±0.0014) MSI −0.0019 (±0.0002)	0. 9323
	OLS	MSI = 1.0586(±0.0022) OLI-2 + 0.0082 (±0.0004)	
	OLS	OLI-2 = 0.8808(±0.0012) MSI + 0.0038 (±0.0002)	

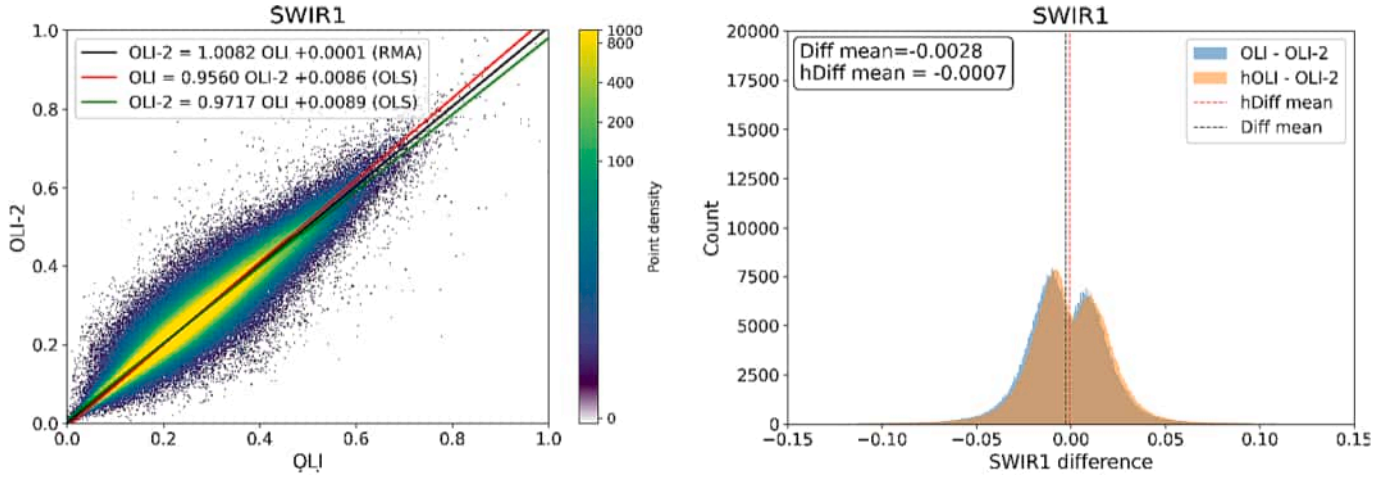

Fig. 9. On the left, the scatterplot of the reflectance values for L9 OLI-2 (vertical axis) against L8 OLI (horizontal axis) in the SWIR1 band (the plot colours illustrate the point density with logarithmic scale; the solid lines show the three regression fits); on the right, the residuals distribution of OLI-2 and OLI applying the RMA coefficients (OLI-2 independent variable) on validation dataset for SWIR1 band, compared with the original paired observation differences (dashed lines represent the mean values). The plots for all the other bands are given in the supplementary materials (SM3 and SM4).

the regression models well explained the variation of reflectance of the dataset, all showing r^2 values higher than 0.90 (p-values < 0.0001). In this case, the r^2 values are lower than those obtained for the L8/L9 cross-sensor analysis, however the red band linear regression is the one with the highest significance also in the S2/L9 fitting. On the other hand, as for the L8/L9 analysis, the lowest r^2 value is registered by the blue band and the same peculiar dispersion in the scatterplot can be seen in Fig. 10a.

As expected, the computed coefficients of the regression are quite stable in the 30 independent sample extractions, as can be observed by looking at the standard deviations reported in Table 5. The highest standard deviation on the slope coefficient is registered in the OLS regression of the blue band having OLI-2 as independent variable.

For validation purpose, the RMA coefficients were applied to all the MSI pixels of the independent validation dataset, in order to compute the hMSI (reflectance values harmonized to the OLI-2). The differences between the transformed reflectance (hMSI) and the original OLI-2 values from the paired observations are computed for every band. Their histogram is shown in Fig. 10 (and SM6), together with the histogram of untransformed differences (MSI-OLI). This time, the beneficial effect of the harmonisation is more evident, and the use of the transformation coefficients allows to translate the curve and concentrate its values on the null mean axis. The bands which benefit more of this harmonization are the blue and the two SWIR bands.

3.1.3. Vegetation indices

As a further assessment of the possible impact of harmonization coefficients computed for single bands, residuals on the four harmonized vegetation indices are presented for both Landsat-8/9 and Sentinel-2/Landsat-9 cross sensor comparisons. Four different VIs were considered in order to compare different combinations of the considered bands, in particular Red, NIR, Blue and SWIR.

The harmonization for the OLI-2/OLI VIs comparison does not modify residuals distribution (Fig. 11), as expected since Landsat-9 was designed as a continuity mission of Landsat-8 (Masek et al., 2020). Conversely, the OLI-2/MSI difference of VIs after the harmonization presented in Fig. 12 shows significant improvements and reduction in the residuals. Moreover, the combination of different bands in the computation of the four indices results in different impacts on the distributions. In general, the computation of VIs with previously harmonized OLI-2 bands significantly reduces sensors differences: mean difference value drops with harmonization from 0.0100 to 0.0008 for NDVI, from 0.0072 to 0.00060 for EVI, from 0.0033 to 0.0001 for SAVI and from 0.0199 to 0.0005 for NDMI. So, as can be seen in Fig. 12, residuals distribution of harmonized VIs is more centred with a mean value equal to zero (red dashed line). The shift in the mean is more evident for NDMI and this is explained by SWIR been the band with highest differences in reflectance value as shown in SM6. For the NDVI, SAVI and EVI indices the distribution of the harmonized difference between sensors is much more symmetric than the original one. In particular, the EVI original difference distribution is the most asymmetric, probably due to the contribution of the blue band.

The presented results highlight the benefits of using the proposed harmonization coefficients, especially when combining different bands into indices.

3.2. Local analyses

3.2.1. In situ surveys

The spectral signatures collected with the spectroradiometer during the field campaigns described in Section 2.3.2 were compared with the L9 and S2 Level-2 products acquired at the same time. The Fig. 13 shows the results of the SAM computed between spectroradiometer survey and image acquisitions, whilst the complete set of similarity indicators is reported in the supplementary materials (SM8).

In general, a good agreement between satellite observations and *in situ* measurements was observed for both S2 and L9 missions, at least in the range of the declared accuracy for Level-2 products (ESA, 2022c). In the majority of the cases, S2 spectra resulted in a better similarity, probably thanks to the finer spatial resolution which reduces the problem of mixed pixels. The single locations perform differently according to different indicators, confirming the importance of considering different metrics. Referring to the results presented in Fig. 13, the mean value of the SAM is 0.07 for the L9 and 0.04 for the S2. Similarly, the SCA mean is 0.06 for L9 and 0.03 for S2 and SID is 0.011 for L9 and 0.003 for S2. Instead, the ED is the only one that shows a mean value very close for both the missions, approximately 0.05 (SM8). These ED values agree with the findings of Pancorbo et al. (2021) who observed a difference in BOA between S2 and field data lower than 4 % in the visible bands, but that analysis was based only on two vegetation covers in a large circular pivot.

Some discrepancies between the observations of the two sensors are probably caused by different atmospheric correction algorithms, estimating atmosphere parameters from different ancillary datasets (Doxani et al., 2018; Marujo et al., 2021). However these differences can be considered low, and are in the majority of cases lower than the declared accuracy, which is ± 5 % for Sentinel Level-2 products (ESA, 2022b). For Landsat Level-2 products, a design accuracy is not stated, but the target accuracy for TOA is ± 3 % (Masek et al., 2020).

Among the 16 surveyed points, only few ones exhibit an anomalous

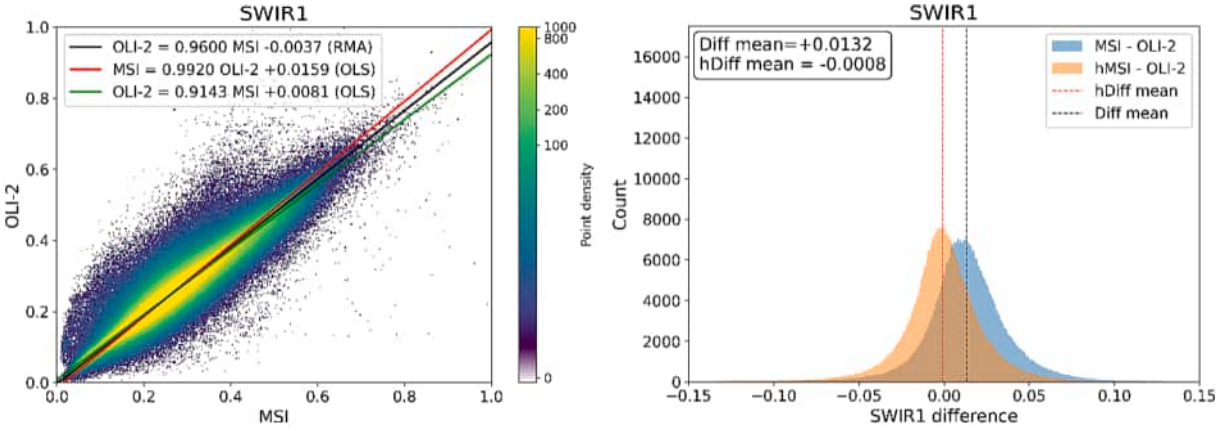

Fig. 10. On the left, the scatterplot of the reflectance values for OLI-2 (vertical axis) against MSI (horizontal axis) in the SWIR1 band (the plot colours illustrate the point density with logarithmic scale; the solid lines show the three regression fits); on the right, the residuals distribution of OLI-2 and MSI applying the RMA coefficients (OLI-2 independent variable) on the validation dataset for SWIR1 band, compared with the original paired observation differences (dashed lines represent the mean values). The plots for all the other bands are given in the supplementary materials (SM5 and SM6).

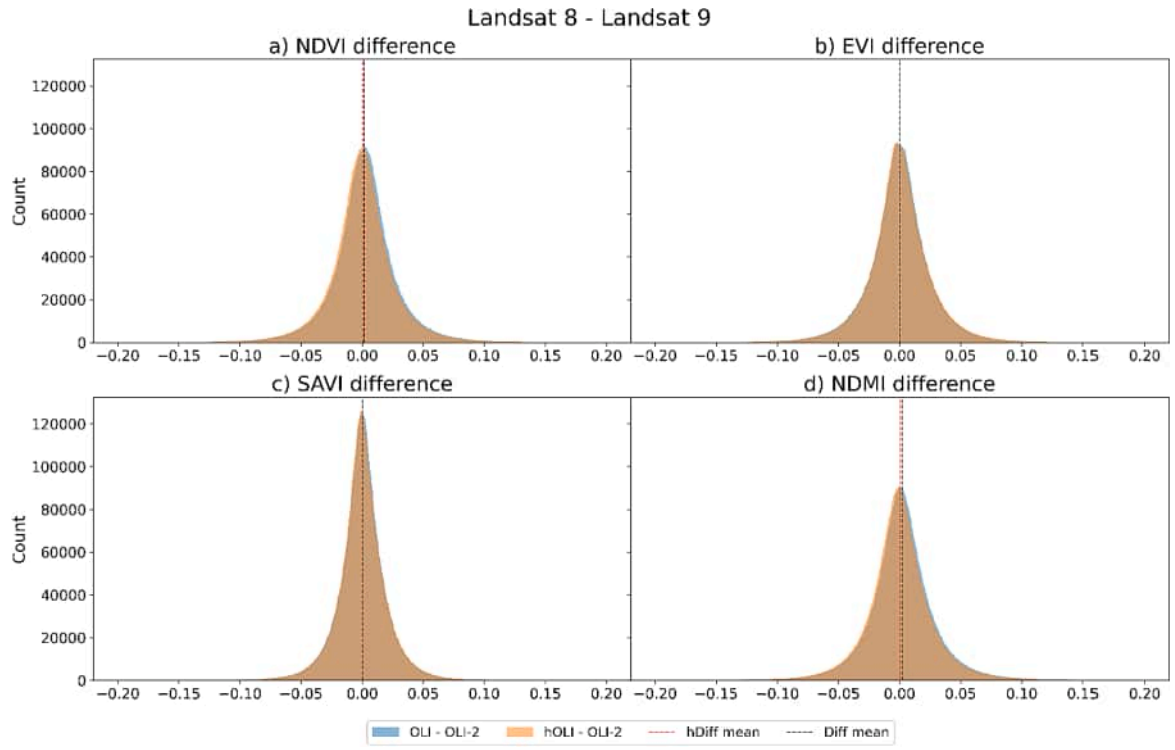

Fig. 11. Distributions of residuals between OLI-2 and OLI derived VIs, applying the RMA coefficients (OLI-2 independent variable), compared with the original VIs differences: NDVI (a), EVI (b), SAVI (c) and NDMI (d).

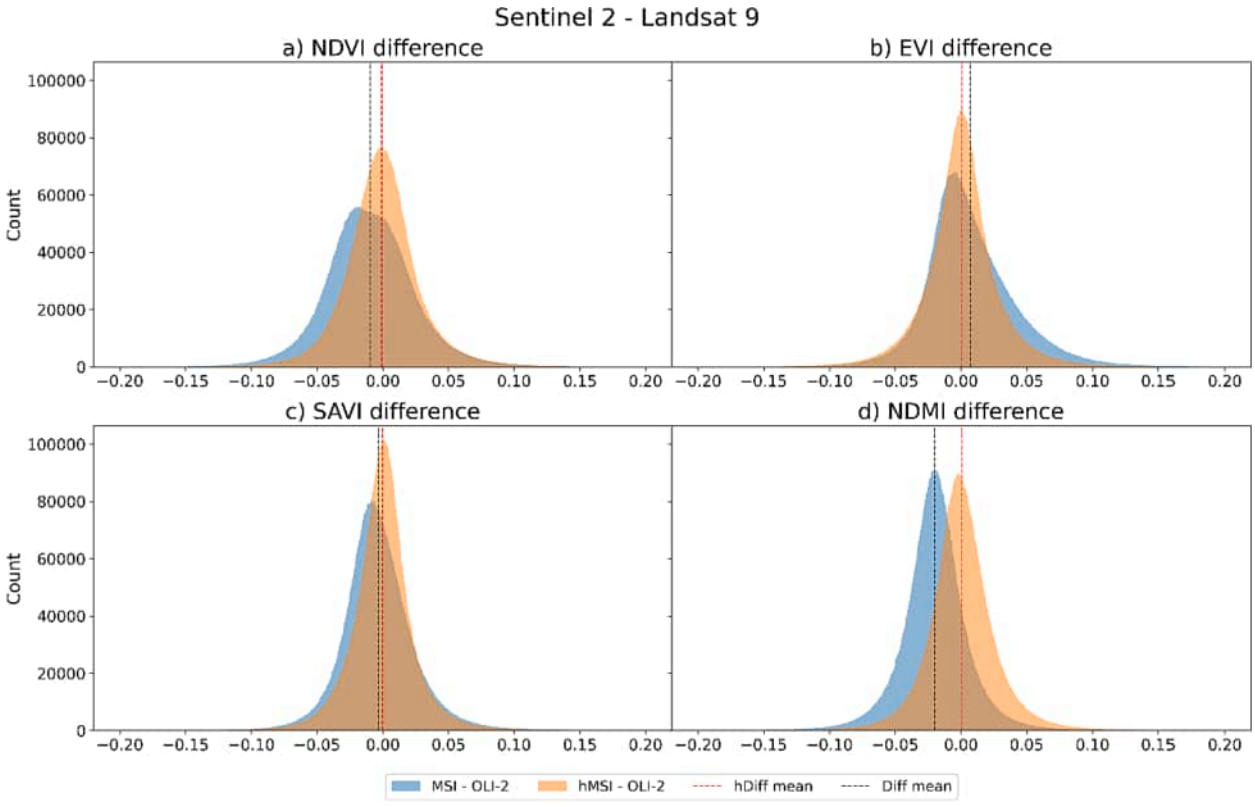

Fig. 12. Distributions of residuals between OLI-2 and MSI derived VIs applying the RMA coefficients (OLI-2 independent variable), compared with the original VIs differences: NDVI (a), EVI (b), SAVI (c) and NDMI (d).

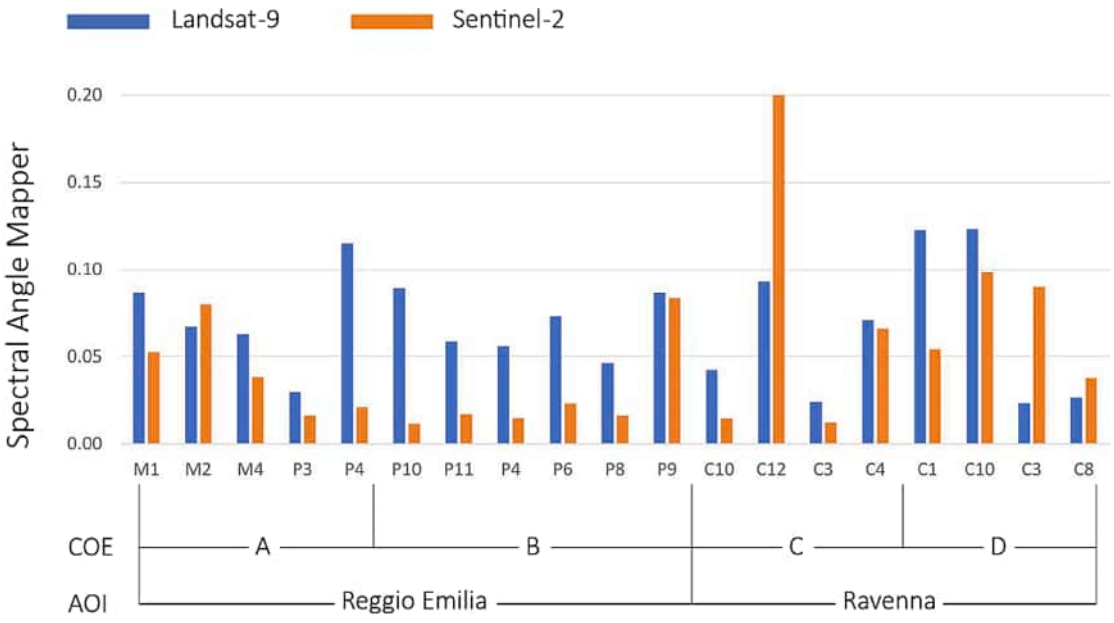

Fig. 13. SAM between the spectra measured on the ground and those extracted by image pixels for all the surveyed locations. The complete set of indicators is reported in supplementary materials (SM8).

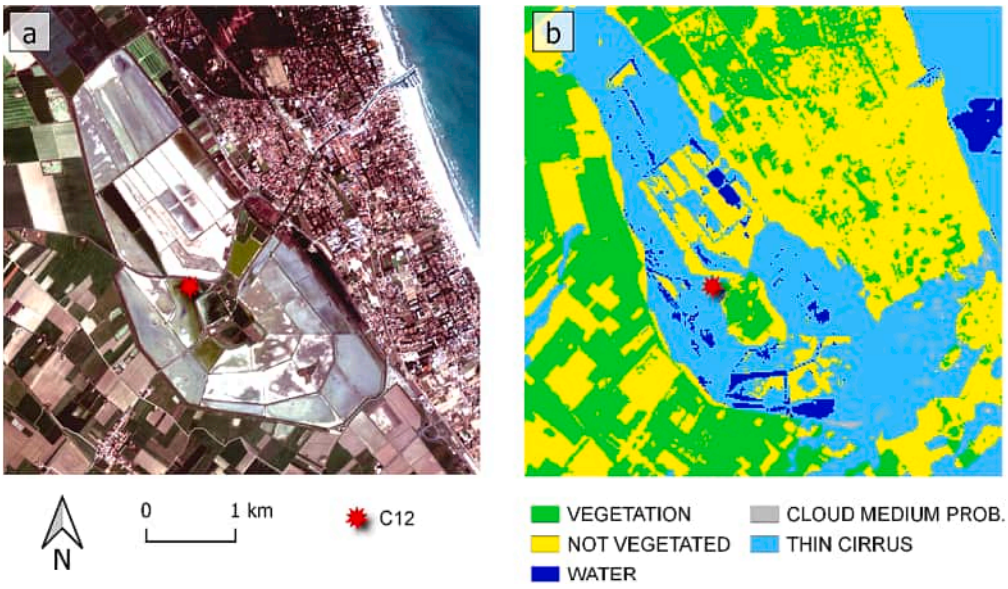

Fig. 14. S2 image of the COE C at C12 sample (salt marshes): (a) true color composite, (b) SCL classification delivered with the Level-2 product. It can be observed that the cirrus class follows the borders of the salt marsh and it is likely misclassified.

behaviour in more than one indicator and thus they were further investigated. In only three points L9 performs significantly better than S2: C3, C12 and M2. A possible explanation of this fact can be given by different atmospheric correction. Indeed, looking at the SCL band of the corresponding S2 image, C3 and C12 pixels are classified as cirrus; the level-2 generation algorithm may in fact over- or under-correct the reflectance values. An example of cirrus misclassification is given in Fig. 14.

It has been already noted in the literature that there are meaningful differences in the cloud detection algorithms used by the two missions (Foga et al., 2017; Louis et al., 2010). Moreover, some authors noted that Sen2cor is less accurate in the detection of clouds (Baetens et al., 2019; Louis et al., 2019).

The problem related to cirrus detection is confirmed by the repetition of the survey in C3 and C10, where only the second date was affected by the cirrus detection resulting in lower performance in all the indicators. The only other point surveyed twice is P4, which shows a different performance of Landsat in the two dates; in this case cloud detection does not seem involved.

4. Conclusion

The cross-comparison between the operating multispectral satellite missions confirmed a very high similarity between Landsat-9 and Landsat-8 and their good interoperability with Sentinel-2 over Europe. In this last case, the harmonization based on a linear transformation proved to be effective in mitigating some discrepancies in the reflectance values of corresponding bands, especially in blue and SWIR bands and even more in derived vegetation indices. These are more pronounced in the Level-2 surface reflectance products, probably due to the different

atmospheric correction algorithms adopted by the two missions. Although some authors offer products reprocessed with a common atmospheric correction algorithm, at the time of the writing they are not available on the mainstream cloud-based geoprocessing platforms. Therefore, the proposed model offers a solution which is easy to implement on official datasets for end-users, also outside the remote sensing experts community.

Local comparisons with *in situ* measurements confirms that in most of the cases the reflectance values derived from the images are within the target accuracy, but some outliers may be caused by inexact detection of cirrus in the generation of Level-2 products or by bi-directional reflectance effects of the surfaces. Also the application of the cubic convolution as a resampling algorithm in the image orthorectification process can cause discrepancies when applied to images with different spatial resolution.

For these reasons, calibration and validation studies are needed, as well as transformation coefficients to harmonize these datasets. In this way, it is possible to perform improved time series analysis of remote sensed data with increased frequency benefitting by these virtual constellation of Landsat/Sentinel data availability, and possibly reducing errors of anomaly detection algorithms. However, this now-verified condition of interoperability is to be monitored throughout the lifetime of the two satellites, as Landsat-8, which is in its 10th year of operation, might be affected in the next years by possible orbital drifts as it happened to its predecessors.

CRediT authorship contribution statement

F. Trevisiol: Methodology, Software, Investigation, Writing – original draft. **E. Mandanici:** Conceptualization, Methodology, Software, Writing – review & editing. **A. Pagliarani:** Data curation, Formal analysis, Validation. **G. Bitelli:** Supervision, Writing – review & editing, Funding acquisition.

Declaration of competing interest

The authors declare that they have no known competing financial interests or personal relationships that could have appeared to influence the work reported in this paper.

Appendix A. Supplementary data

Supplementary data to this article can be found online at https://doi.org/10.1016/j.isprsjprs.2024.02.021.

References

Baetens, L., Desjardins, C., Hagolle, O., 2019. Validation of copernicus Sentinel-2 cloud masks obtained from MAJA, Sen2Cor, and FMask processors using reference cloud masks generated with a supervised active learning procedure. Remote Sens. (Basel) 11 (4), 433. https://doi.org/10.3390/rs11040433.

Brown, C.F., Brumby, S.P., Guzder-Williams, B., Birch, T., Hyde, S.B., Mazzariello, J., Czerwinski, W., Pasquarella, V.J., Haertel, R., Ilyushchenko, S., Schwehr, K., Weisse, M., Stolle, F., Hanson, C., Guinan, O., Moore, R., Tait, A.M., 2022. Dynamic world, near real-time global 10 m land use land cover mapping. Sci. Data 9 (1), 1–17. https://doi.org/10.1038/s41597-022-01307-4.

Campbell, J.W., Aarup, T., 1989. Photosynthetically available radiation at high latitudes. Limnol. Oceanogr. 34 (8), 1490–1499. https://doi.org/10.4319/lo.1989.34.8.1490.

Chang, C.-I., 2000. An information-theoretic approach to spectral variability, similarity, and discrimination for hyperspectral image analysis. IEEE Trans. Inf. Theory 46 (5), 1927–1932. https://doi.org/10.1109/18.857802.

Chastain, R., Housman, I., Goldstein, J., Finco, M., Tenneson, K., 2019. Empirical cross sensor comparison of sentinel-2A and 2B MSI, Landsat-8 OLI, and Landsat-7 ETM+ top of atmosphere spectral characteristics over the conterminous United States. Remote Sens. Environ. 221, 274–285.

E. D. Chaves, M.; C. A. Picoli, M.; D. Sanches, I. Recent Applications of Landsat 8/OLI and Sentinel-2/MSI for Land Use and Land Cover Mapping: A Systematic Review. *Remote Sens.* 2020, *12*, 3062. https://doi.org/10.3390/rs12183062.

Claverie, M., Ju, J., Masek, J.G., Dungan, J.L., Vermote, E.F., Roger, J.-C., Skakun, S.V., Justice, C., 2018. The harmonized landsat and Sentinel-2 surface reflectance data set. Remote Sens. Environ. 219, 145–161. https://doi.org/10.1016/j.rse.2018.09.002.

Spectra Vista Corporation - SVC. (2019). Field Spectroscopy Guide with SVC i-series Spectroradiometers.

Doxani, G., Vermote, E., Roger, J.-C., Gascon, F., Adriaensen, S., Frantz, D., Hagolle, O., Hollstein, A., Kirches, G., Li, F., Louis, J., Mangin, A., Pahlevan, N., Pflug, B., Vanhellemont, Q., 2018. Atmospheric correction inter-comparison exercise. Remote Sensing 10 (3), 352. https://doi.org/10.3390/rs10020352.

ESA - European Space Agency. (2015). Sentinel-2 Processing Baseline. https://sentinels.copernicus.eu/web/sentinel/technical-guides/sentinel-2-msi/processing-baseline.

ESA. (2015). SENTINEL-2 User Handbook. 1, 64. https://doi.org/GMES-S1OP-EOPG-TN-13-0001.

ESA. (2022). S2 MPC Level 2A - Data quality report.

ESA - European Space Agency. (2022a). Data Quality Report - MSI L2A - January 2022. In Sentinel Online - Data Product Quality Reports (Issue 46.0 January). https://sentinels.copernicus.eu/web/sentinel/data-product-quality-reports.

ESA - European Space Agency. (2022b). Data Quality Report - MSI L2A - May 2022. Sentinel Online -Data Product Quality Reports, May. https://sentinels.copernicus.eu/web/sentinel/data-product-quality-reports.

Foga, S., Scaramuzza, P.L., Guo, S., Zhu, Z., Dilley, R.D., Beckmann, T., Schmidt, G.L., Dwyer, J.L., Joseph Hughes, M., Laue, B., 2017. Cloud detection algorithm comparison and validation for operational landsat data products. Remote Sens. Environ. 194, 379–390. https://doi.org/10.1016/j.rse.2017.03.026.

Ghaderpour, E., Vujadinovic, T., 2020. Change detection within remotely sensed satellite image time series via spectral analysis. Remote Sens. (Basel) 12 (23), 4001. https://doi.org/10.3390/rs12234001.

Gorelick, N., Hancher, M., Dixon, M., Ilyushchenko, S., Thau, D., Moore, R., 2017. Google earth engine: planetary-scale geospatial analysis for everyone. Remote Sens. Environ. 202, 18–27.

Gross, G., Helder, D., Begeman, C., Leigh, L., Kaewmanee, M., Shah, R., 2022. Initial cross-calibration of landsat 8 and landsat 9 using the simultaneous underfly event. Remote Sens. (Basel) 14 (10). https://doi.org/10.3390/rs14102418.

Harper, W.V. (2016). Reduced Major Axis Regression. In Wiley StatsRef: Statistics Reference Online (pp. 1–6). Wiley. https://doi.org/10.1002/9781118445112.stat07912.

Helder, D., Markham, B., Morfitt, R., Storey, J., Barsi, J., Gascon, F., Clerc, S., LaFrance, B., Masek, J., Roy, D.P., Lewis, A., Pahlevan, N., 2018. Observations and recommendations for the calibration of landsat 8 OLI and sentinel 2 MSI for improved data interoperability. Remote Sens. (Basel) 10 (9), 1–29. https://doi.org/10.3390/rs10091340.

Kaufman, Y.J., Sendra, C., 1988. Algorithm for automatic atmospheric corrections to visible and near-IR satellite imagery. Int. J. Remote Sens. 9 (8), 1357–1381. https://doi.org/10.1080/01431168808954942.

Kruse, F.A., Lefkoff, A.B., Boardman, J.W., Heidebrecht, K.B., Shapiro, A.T., Barloon, P. J., Goetz, A.F.H., 1993. The spectral image processing system (SIPS)-interactive visualization and analysis of imaging spectrometer data. AIP Conf. Proc. 283, 192–201. https://doi.org/10.1063/1.44433.

Li, J., Chen, B., 2020. Global revisit interval analysis of Landsat-8 -9 and sentinel-2A -2B data for terrestrial monitoring. Sensors 20 (22), 6631. https://doi.org/10.3390/s20226631.

Li, J., Roy, D.P., 2017. A global analysis of sentinel-2a, sentinel-2b and Landsat-8 data revisit intervals and implications for terrestrial monitoring. Remote Sens. (Basel) 9 (9). https://doi.org/10.3390/rs9090902.

Louis, J., Charantonis, A., Berthelot, B., Lacoste-Francis, H., 2010. Cloud detection for Sentinel-2. Living Planet Symposium Proceedings 686, 499. https://www.tib.eu/de/suchen/id/BLCP%3ACN078005293.

Louis, J., Pflug, B., Main-Knorn, M., Debaecker, V., Mueller-Wilm, U., Iannone, R.Q., Giuseppe Cadau, E., Boccia, V., Gascon, F., 2019. Sentinel-2 global surface reflectance level-2a product generated with Sen2Cor. In: IGARSS 2019–2019 IEEE International Geoscience and Remote Sensing Symposium, pp. 8522–8525. https://doi.org/10.1109/IGARSS.2019.8898540.

Main-Knorn, M., Pflug, B., Louis, J., Debaecker, V., Müller-Wilm, U., & Gascon, F. (2017). Sen2Cor for Sentinel-2. In L. Bruzzone, F. Bovolo, & J. A. Benediktsson (Eds.), Image and Signal Processing for Remote Sensing XXIII (p. 3). SPIE. https://doi.org/10.1117/12.2278218.

Mandanici, E., Bitelli, G., 2016. Preliminary comparison of Sentinel-2 and landsat 8 imagery for a combined use. Remote Sens. (Basel) 8 (12), 1014. https://doi.org/10.3390/rs8121014.

Marujo, R.F.B., Fronza, J.G., Soares, A.R., Queiroz, G.R., Ferreira, K.R., 2021. Evaluating the impact of lasrc and SEN2COR atmospheric correction algorithms on Landsat-8/OLI and Sentinel-2/MSI data over aeronet stations in brazilian territory. ISPRS Annals of the Photogrammetry, Remote Sensing and Spatial Information Sciences 5 (3), 271–277. https://doi.org/10.5194/isprs-annals-V-3-2021-271-2021.

Masek, J.G., Wulder, M.A., Markham, B., McCorkel, J., Crawford, C.J., Storey, J., Jenstrom, D.T., 2020. Landsat 9: empowering open science and applications through continuity. Remote Sens. Environ. 248 (April), 111968 https://doi.org/10.1016/j.rse.2020.111968.

Naresh Kumar, M., Seshasai, M.V.R., Vara Prasad, K.S., Kamala, V., Ramana, K.V., Dwivedi, R.S., Roy, P.S., 2011. A new hybrid spectral similarity measure for discrimination among vigna species. Int. J. Remote Sens. 32 (14), 4041–4053. https://doi.org/10.1080/01431161.2010.484431.

Pahlevan, N., Sarkar, S., Franz, B.A., Balasubramanian, S.V., He, J., 2017. Sentinel-2 MultiSpectral instrument (MSI) data processing for aquatic science applications: demonstrations and validations. Remote Sens. Environ. 201, 47–56. https://doi.org/10.1016/j.rse.2017.08.033.

Pancorbo, J.L., Lamb, B.T., Quemada, M., Hively, W.D., Gonzalez-Fernandez, I., Molina, I., 2021. Sentinel-2 and WorldView-3 atmospheric correction and signal normalization based on ground-truth spectroradiometric measurements. ISPRS J.

Photogramm. Remote Sens. 173, 166–180. https://doi.org/10.1016/j.isprsjprs.2021.01.009.
Qiu, S., Zhu, Z., Shang, R., Crawford, C.J., 2021. Can landsat 7 preserve its science capability with a drifting orbit? Science of Remote Sensing 4, 100026. https://doi.org/10.1016/j.srs.2021.100026.
Robila, S.A., & Gershman, A. (2005). Spectral matching accuracy in processing hyperspectral data. International Symposium on Signals, Circuits and Systems, 2005. ISSCS 2005., 1, 163–166. https://doi.org/10.1109/ISSCS.2005.1509878.
Roitberg, E., Malgeac, I., Weil-Zattelman, S., Kizel, F., 2022. BRDF laboratory measurements using a camera-aided spectroradiometer. Int. Arch. Photogramm. Remote. Sens. Spat. Inf. Sci. XLIII-B3-2, 417–422. https://doi.org/10.5194/isprs-archives-XLIII-B3-2022-417-2022.
Roy, D.P., Kovalskyy, V., Zhang, H.K., Vermote, E.F., Yan, L., Kumar, S.S., Egorov, A., 2016. Characterization of Landsat-7 to Landsat-8 reflective wavelength and normalized difference vegetation index continuity. Remote Sens. Environ. 185, 57–70. https://doi.org/10.1016/j.rse.2015.12.024.
Schläpfer, D., Borel, C.C., Keller, J., Itten, K.I., 1998. Atmospheric precorrected differential absorption technique to retrieve columnar water vapor. Remote Sens. Environ. 65 (3), 353–366. https://doi.org/10.1016/S0034-4257(98)00044-3.
Teixeira Pinto, C., Jing, X., Leigh, L., 2020. Evaluation analysis of landsat Level-1 and Level-2 data products using in situ measurements. Remote Sens. (Basel) 12 (16), 2597. https://doi.org/10.3390/rs12162597.
Trevisiol, F., Mattivi, P., Mandanici, E., Bitelli, G., 2024. Cross-Sensors Comparison of Popular Vegetation Indexes From Landsat TM, ETM=, OLI, and Sentinel MSI for Time-Series Analysis Over Europe. IEEE Transactions on Geoscience and Remote Sensing 62, 1–16. https://doi.org/10.1109/tgrs.2023.3343071.
U.S. Geological Survey. (2019). Landsat 8 Data Users Handbook (Vol. 8, Issue November). https://landsat.usgs.gov/documents/Landsat8DataUsersHandbook.pdf.
U.S. Geological Survey. (2021). Landsat collection 2. In Fact Sheet (Version 1.). https://doi.org/10.3133/fs20213002.
U.S. Geological Survey. (2022a). Landsat-9 data processing resumes. https://www.usgs.gov/landsat-missions/news/landsat-9-data-processing-resumes.
U.S. Geological Survey. (2022b). Landsat 9 Data Users Handbook (Issue February). https://d9-wret.s3.us-west-2.amazonaws.com/assets/palladium/production/s3fs-public/media/files/LSDS-2082_L9-Data-Users-Handbook_v1.pdf.
Vermote, E., Justice, C., Claverie, M., Franch, B., 2016. Preliminary analysis of the performance of the landsat 8/OLI land surface reflectance product. Remote Sens. Environ. 185, 46–56. https://doi.org/10.1016/j.rse.2016.04.008.
Wu, Z., Snyder, G., Vadnais, C., Arora, R., Babcock, M., Stensaas, G., Doucette, P., Newman, T., 2019. User needs for future landsat missions. Remote Sens. Environ. 231 (May), 111214 https://doi.org/10.1016/j.rse.2019.111214.
Wulder, M.A., Loveland, T.R., Roy, D.P., Crawford, C.J., Masek, J.G., Woodcock, C.E., Allen, R.G., Anderson, M.C., Belward, A.S., Cohen, W.B., Dwyer, J., Erb, A., Gao, F., Griffiths, P., Helder, D., Hermosilla, T., Hipple, J.D., Hostert, P., Hughes, M.J., Huntington, J., Johnson, D.M., Kennedy, R., Kilic, A., Li, Z., Lymburner, L., McCorkel, J., Pahlevan, N., Scambos, T.A., Schaaf, C., Schott, J.R., Sheng, Y., Storey, J., Vermote, E., Vogelmann, J., White, J.C., Wynne, R.H., Zhu, Z., 2019. Current status of landsat program, science, and applications. Remote Sens. Environ. 225, 127–147.
Wulder, M.A., Hermosilla, T., White, J.C., Hobart, G., Masek, J.G., 2021. Augmenting landsat time series with harmonized landsat Sentinel-2 data products: assessment of spectral correspondence. Science of Remote Sensing 4, 100031. https://doi.org/10.1016/j.srs.2021.100031.
Wulder, M.A., Roy, D.P., Radeloff, V.C., Loveland, T.R., Anderson, M.C., Johnson, D.M., Healey, S., Zhu, Z., Scambos, T.A., Pahlevan, N., Hansen, M., Gorelick, N., Crawford, C.J., Masek, J.G., Hermosilla, T., White, J.C., Belward, A.S., Schaaf, C., Woodcock, C.E., Huntington, J.L., Lymburner, L., Hostert, P., Gao, F., Lyapustin, A., Pekel, J.-F., Strobl, P., Cook, B.D., 2022. Fifty years of landsat science and impacts. Remote Sens. Environ. 280, 113195.
Zhang, H.K., Roy, D.P., 2016. Landsat 5 thematic mapper reflectance and NDVI 27-year time series inconsistencies due to satellite orbit change. Remote Sens. Environ. 186, 217–233. https://doi.org/10.1016/j.rse.2016.08.022.